Taylor & Francis
Taylor & Francis Group

Science and Technology of Advanced Materials: Methods

ISSN: 2766-0400 (Online) Journal homepage: www.tandfonline.com/journals/tstm20

Computational material screening for electrode materials of BaSi solar cells

Tomoaki Yazaki, Keisuke Arimoto, Junji Yamanaka & Kosuke O. Hara

To cite this article: Tomoaki Yazaki, Keisuke Arimoto, Junji Yamanaka & Kosuke O. Hara (28 Jan 2026): Computational material screening for electrode materials of BaSi solar cells, Science and Technology of Advanced Materials: Methods, DOI: 10.1080/27660400.2026.2617671

To link to this article: https://doi.org/10.1080/27660400.2026.2617671

We present a high-throughput screening workflow integrating device simulations and property computations, enabling rapid identification of promising electrode materials for $BaSi_2$ and broader photovoltaic technologies.

Computational material screening for electrode materials of $BaSi_2$ solar cells

Tomoaki Yazaki[a], Keisuke Arimoto[a], Junji Yamanaka[a], and Kosuke O. Hara[b]
[a]University of Yamanashi, 7-32 Miyamae, Kofu, Yamanashi, Japan;
[b]Nara Institute of Science and Technology, 8916-5 Takayama, Ikoma, 630-0192, Nara, Japan

ARTICLE HISTORY
Compiled January 8, 2026

ABSTRACT
In this study, we developed a computational material screening workflow for metallic electrodes of $BaSi_2$ solar cells. Elemental and binary metallic materials in the Materials Project database were screened for four device models with different charge transport layer materials contacting the electrode. The screening criteria included chemical stability, melting point, and work function. In contrast to conventional screening approaches that rely solely on materials descriptors, the present workflow explicitly incorporates device-level performance constraints by using the relationship between the work function and the simulated power conversion efficiency. For melting point evaluation, a linear regression estimation from the cohesive energy and a machine learning model were compared to assess their accuracy, which revealed the higher accuracy of the machine learning model. For work function evaluation, first-principles calculation and another machine learning model were compared, which showed similar accuracies. Considering the computational cost, the machine learning model was used for screening. The threshold of work function screening was determined by device simulations. As a result, promising materials for metallic electrodes were successfully identified. Moreover, the developed screening workflow with high versatility will be applicable to material discovery for other solar cells and semiconductor devices.

KEYWORDS
Solar cells; Metallic electrode; High-throughput virtual screening; Work function; Melting point; Density functional theory

CONTACT T. Yazaki Author. Email: tyazaki617@g.chuo-u.ac.jp
CONTACT K. O. Hara Author. Email: hara.kosuke@naist.ac.jp

1. Introduction

The selection of appropriate electrode materials is crucial for improving the performance of electronic and energy conversion devices, such as solar cells, thermoelectric devices, and MOSFETs [1–7]. In particular, the metallic electrode of a solar cell significantly affects carrier transport efficiency, thereby influencing the overall power conversion efficiency (PCE). Additionally, it is essential to have a high melting point (T_m) to withstand high temperature growth and annealing of upper layers and to prevent unintended chemical reactions at the interface. It is challenging to identify optimal electrode materials by comprehensively considering band alignment, T_m, and chemical reactivity.

The conventional selection of metallic materials has been based on empirical rules and trial-and-error methods, making it challenging to comprehensively evaluate multidimensional material properties. Additionally, the material search space was limited, restricting the number of materials considered. Computational material screening is a powerful approach that screens a huge set of data in databases based on computed properties [8]. This approach can accelerate the discovery of ideal materials in a rational way.

The focus of this study is the metallic electrode of $BaSi_2$ solar cells. $BaSi_2$ has a band gap (E_g) of 1.3 eV, high optical absorption coefficients ($\geq 10^4$ cm^{-1} for photon energies over E_g) [9–11], and long minority carrier lifetime (up to 27 μs) [12–14], making it a promising light-absorbing material for solar cells. However, the maximum PCE of $BaSi_2$ solar cells reported to date remains around 10% [15], which is partly attributed to the lack of an optimized device structure. In particular, $BaSi_2$ has a relatively low electron affinity of 3.2 eV [16] compared to other solar cell absorbers, making it difficult to use the device architectures of other solar cells.

In previous studies, we adopted a double heterojunction structure and searched for materials for the electron transport layer (ETL) and hole transport layer (HTL) by computational material screening, successfully identifying optimal materials [17]. The most promising materials among them include Sm_2O_3, 6H-SiC, and 4H-SiC for ETL and BaS for HTL because of the best band alignment, compositional simplicity, and synthesizability. Our screening workflow is unique in that it relies not only on material descriptors but also on device-level performance constraints. This allows us to estimate the expected PCE with the selected materials. The estimated PCE with the identified materials exceeded 30%. The thin film deposition processes for these layers are currently being developed [18, 19]. However, suitable materials for the transparent conductive electrode and back metal electrode have not been explored. In particular, the selection of an appropriate back electrode material poses a challenge due to the large number of candidate materials compared to transparent conductive materials.

In this study, we develop a device-simulation-coupled computational material screening procedure for metallic electrodes to identify the optimal electrode materials for double heterojunction $BaSi_2$ solar cells. Particular focus is on T_m and work function (ϕ_m). T_m screening is desirable for $BaSi_2$ solar cells because the optical properties of $BaSi_2$ are improved by annealing at 850–1000 °C [20], requiring materials with high T_m. Two methods are investigated for rapidly and accurately estimating T_m and ϕ_m. Based on the result, an effective procedure of computational material screening is proposed for electrode materials of solar cells. Because the ETL and HTL materials contacting the electrode affect the screening results, we studied four different device structures with Sm_2O_3, 6H-SiC, and 4H-SiC as ETL materials and BaS as the HTL material in this study. Promising candidate materials are identified for different device structures.

2. Methods

2.1. *Device simulations*

Device simulations were conducted using the console version of wxAMPS [21, 22] under AM 1.5 illumination with an intensity of 1000 $\mathrm{W/m^2}$ to investigate the required conditions for the ϕ_m of the electrode materials. Four device models shown in Fig. 1 were investigated. All four models consist of transparent conductive film (TCF, 100 nm), HTL (100 nm), $BaSi_2$ (2 μm [17]), ETL (100 nm), and metallic electrode. Three of the models have ETL at the back side, contacting with metallic electrodes, while the other one has HTL at the back side. The ETL materials selected were Sm_2O_3, 4H-SiC, and 6H-SiC, while BaS was chosen for HTL.

The material properties were basically referenced from literatures, as summarized in Table 1. Absorption coefficients of $BaSi_2$ were taken from Ref. [23] with neglecting the values for photon energies below E_g. However, the absorption coefficients for ETL, HTL, and TCF were assumed for simplicity to be step functions, which were 10^5 $\mathrm{cm^{-1}}$ for photon energies over E_g, and zero otherwise. Electron densities in $BaSi_2$ and ETL were assumed to be 1×10^{16} $\mathrm{cm^{-3}}$ [24–26] and 1×10^{14} $\mathrm{cm^{-3}}$, respectively, while hole density in HTL was assumed to be 1×10^{14} $\mathrm{cm^{-3}}$. The conductivity type of TCF was assumed to be either n- or p-type when contacting with ETL or HTL, respectively, with carrier density of 1×10^{21} $\mathrm{cm^{-3}}$.

For $BaSi_2$, the effective density of states in the conduction band (N_C), the effective density of states in the valence band (N_V), and the radiative recombination coefficient (B) are $N_C = 6.76\times10^{18}$ $\mathrm{cm^{-3}}$, $N_V = 1.07\times10^{19}$ $\mathrm{cm^{-3}}$, and $B = 1.09\times10^{-11}$ $\mathrm{cm^3\ s^{-1}}$ [17]. These values were also used for ETL, HTL, and TCF.

All carrier mobilities were assumed to be 100 $\mathrm{cm^2\,V^{-1}\,s^{-1}}$. The dielectric constant of TCF was assumed to be the same as $BaSi_2$. The E_g and electron affinity of TCF were set to the optimal values that maximize PCE for given models. The front- and back-side reflectances were set to 0 and 1, respectively. The effective surface recombination velocities for both the front and back sides were assumed to be 10^7 cm/s. Bulk defects and band tailing were not considered, and the intraband tunneling mode was employed as the simulation mode.

Metal electrodes were not explicitly included in the models. Instead, effects of different ϕ_m were considered by different potential barrier heights (PBH) at the back surfaces. For the ETL/metal electrode interface, PBH corresponds to the difference between the ϕ_m of the electrode and the electron affinity of ETL, while for the HTL/electrode interface, PBH corresponds to the difference between the ϕ_m of the electrode and the ionization potential of HTL.

2.2. *Computational material screening*

The Materials Project database [27] was screened using the mp-api and pymatgen [28] Python library (access in June 2023). The search space was limited to single and binary compounds free from rare (less abundant than Ag in the Earth's crust), highly toxic (Be, Cd, As, Hg, Pb, Tl), and radioactive elements. Only metallic materials were included by setting $E_g = 0$ eV. Additionally, to ensure the stability of the materials, we applied the condition that the energy above the convex hull $= 0$ eV.

First, we evaluated interfacial chemical reactivity. The interfacial chemical reactivity was evaluated using the InterfacialReactivity class [30] of pymatgen. We excluded the materials

that can thermodynamically react with the adjacent layer.

T_m was evaluated by two methods to find out a rapid and accurate method that is suitable for high-throughput screening. One is based on the relationship between the T_m and cohesive energies (E_{coh}). The E_{coh} of compounds was calculated by Miedema's theory using Miedema.py [31, 32]. Linear regression was analyzed between the E_{coh} and the "temperature for congruent melting" data from the Materials Platform for Data Science (MPDS) for randomly selected 93 binary compounds. The intercept was set to zero. This regression line allowed us to estimate the T_m. The other method uses a machine learning model developed by Hong *et al.* [33]. This machine learning model was trained on approximately 10,000 compound data [33], and predicts a T_m using a graph neural network and a residual neural network. The accuracies of these methods were evaluated by the prediction errors for different randomly selected data from MPDS.

Appropriate estimation methods for ϕ_m were also investigated. We compared the density functional theory (DFT) and machine learning methods using the experimental work function data [34] for elemental metals as reference. We used Quantum Espresso [35, 36] for DFT calculations. ϕ_m was estimated as the difference between the Fermi and vacuum levels using slab models of thicker than 20 Å with 20 Å vacuum regions. Slab models were generated using the pymatgen library [37, 28]. If slabs with several different surface terminations were prepared, their ϕ_m were averaged. All calculations were performed with the Perdew–Burke–Ernzerhof functional tuned for solids (PBEsol) [38] in the generalized gradient approximation (GGA). ϕ_m were estimated after structural relaxation. Gaussian smearing with the spreading of 68 meV was used for occupations. We followed our previous papers [26, 17] for other parameter settings. The machine learning model for ϕ_m investigated was the random forest model developed by Schindler *et al.* [39]. This model was trained on a dataset comprising 58,332 ϕ_m and 33,631 exfoliation energies obtained from high-throughput DFT calculations. In this study, we averaged ϕ_m over different surface terminations to obtain a representative ϕ_m for a given crystal plane. This approach was adopted because identifying the most probable termination for each material is impractical, even though actual surface terminations depend on crystal growth conditions. ϕ_m of 33 elemental metals were evaluated by both methods, and the accuracy was evaluated using the experimentally reported ϕ_m [34] as reference values.

3. Results and discussion

3.1. *Device simulations*

Figures 2(a) and 2(b) show the band alignments of the model (C) in Fig. 1 under dark conditions with PBH = 0.0 and 0.5 eV, respectively. In the figures, the metallic electrode is assumed to be present on the right side of the Sm_2O_3 ETL. Obviously, this band alignment with PBH = 0.0 eV allows efficient charge separation with small potential barriers for electrons toward the back electrode through Sm_2O_3 ETL (0.26 eV) and for holes toward the front TCF through BaS HTL (0.15 eV). On the other hand, with PBH = 0.5 eV, the band energy levels of ETL and $BaSi_2$ near ETL rise toward the back electrode. This band bending obstructs electron transport and reduces PCE. To identify the ϕ_m range where smooth charge transport is assured, PCE was simulated with different PBH values.

Figures 3(a)–(d) show the PCE as functions of ϕ_m of metallic electrodes for the models (A)–(D) in Fig. 1, respectively. The horizontal dashed line in each panel of Fig. 3 indicates a

PCE of 30%. With the models (A)–(C), PCE decreases with increasing ϕ_m. This is because the band energy levels of the ETL and $BaSi_2$ near ETL increase, as shown in the insets. The thresholds of the ϕ_m where PCE starts to decrease are 3.90, 3.61, and 3.32 eV for the models (A)–(C), respectively. These thresholds corresponding to PBH of 0.3 eV, which is presumably the highest barrier that electrons can overcome. On the other hand, with the model (D), PCE decreases with decreasing ϕ_m, because the band energy levels are lowered and the barriers for holes are generated. The threshold where PCE starts to decrease is 4.42 eV, which again corresponds to the PBH of 0.3 eV for holes. This 0.3 eV PBH threshold is a useful criterion that could be applicable to various types of solar cells. For the purpose of electrode materials selection of this study, the ϕ_m thresholds serve as criteria for computational material screening.

3.2. *Computational material screening*

The workflow of computational material screening for metallic electrode materials is shown in Fig. 4. The search space was defined by $E_g = 0$ eV, the energy above the convex hull $= 0$ eV, and elemental and binary substances without rare, toxic, and radioactive elements described in Methods. At this stage, 1,830 metallic materials were included in the candidate list. The interface reactivity screening decreased the number of candidates to 567, 567, 878, and 1483 for models (A)–(D), respectively. To further screen the materials by T_m, we compared two estimation methods to select an appropriate method: linear regression using Miedema's E_{coh} and the machine learning model.

The physical principle of melting indicates that a high E_{coh} leads to a high T_m, which is the basis of estimating T_m from E_{coh}. Actually, T_m is reported to be roughly proportional to E_{coh} in Laves phases [31]. We determined the regression line between E_{coh} and T_m using the data for random binary metallic compounds in MPDS. E_{coh} was calculated using Miedema's theory [40, 31]. Figure 5 shows the T_m plotted against E_{coh} together with the regression line. A positive correlation is confirmed between T_m and E_{coh}. The coefficient of determination was 0.85 according to Kvålseth's R_2^8 definition [41]. The obtained regression equation is $(T_m / \mathrm{K}) = 5.27 \times (E_{coh} / \mathrm{kJmol^{-1}})$.

Figure 6 compares the T_m estimated using the regression line derived from E_{coh} and those predicted by the machine learning model developed by Hong *et al* [33], with the reference values obtained from MPDS. Different material data were used from those used for the linear regression. The accuracy of the T_m estimation was evaluated using the mean absolute error (MAE). The MAE of the linear regression was 616.7 K, while that of the machine learning model was 69.6 K, showing the higher accuracy of the machine learning model than the linear regression method. The estimation based on E_{coh} is reported effective for materials with specific structures, such as Laves phases [31]. The current evaluation indicates that the simple linear regression is not as effective as machine learning for materials with various crystal structures. Therefore, we employed the machine learning model [33] for T_m estimation.

We screened the candidate materials with the T_m criterion of 1000 °C because annealing at 1000 °C is reported to enhance the photoresponsivity of $BaSi_2$ [20], and hence, the metallic electrode is possibly exposed to high temperatures up to 1000 °C during solar cell fabrication. After the T_m screening step, 388, 388, 624, and 1136 candidates were retained for models (A)–(D) in Fig. 1, respectively.

The last screening step involved ϕ_m, which is the essential parameter influencing the PCE, as shown in Fig. 3. DFT is the most reliable method to computationally estimate the ϕ_m of materials, while Schindler *et al.* recently reported a machine learning model using random forest for ϕ_m prediction [39]. We investigated the prediction accuracy of these two methods by estimating the ϕ_m of 33 elemental metals using the reported experimental values [34] as reference.

Figure 7 shows the ϕ_m of elemental metals estimated by DFT and the machine learning model. The (100) surface was selected for all metals. The average ϕ_m of different surface terminations is shown. The MAEs between the estimated and reference values was 0.30 eV for DFT and 0.31 eV for the machine learning model. This result indicates that both methods estimate the ϕ_m with similar accuracy. This is possibly because the machine learning model was trained on the DFT calculation data, leading to a prediction error comparable to that of DFT. The data used to train the machine learning model were prepared with ionically unrelaxed slabs, while our DFT calculations involved ionic relaxations of slab models. Regardless of this difference, the machine learning model worked well. Additionally, computational costs are greatly lower with the machine learning model than DFT. Therefore, screening was conducted using the machine learning model [39].

To represent the work function of a polycrystalline surface, work functions calculated by the machine learning model for inequivalent surface planes were averaged. Miller indices up to 1 were considered. In principle, a weighted average that accounts for the exponential dependence of thermionic emission on the work function should be used, with the fractional areas as weights [42]. However, these fractional areas cannot be reliably estimated. Therefore, we adopted a simple arithmetic average over inequivalent crystal planes. To assess the validity of this approach, we evaluated the work functions of 43 polycrystalline elements, for which experimental polycrystalline values are available [34]. The resulting MAE was 0.26 eV, comparable to that obtained for the (100) surface. This result indicates that averaging over inequivalent planes provides sufficient accuracy for screening purposes.

The ϕ_m screening was performed with the criterion that the PCE should exceed 30%, which was derived from the simulation results shown in Fig. 3. This step resulted in 197, 89, 41, and 233 candidates for the models (A)–(D) in Fig.1, respectively. These final candidates and their properties are summarized in Table 2–5.

When the ETL was placed on the back side [models (A)–(C)], the number of candidate materials was smaller than otherwise [model (D)]. This is due to the imposed conditions of high T_m and low ϕ_m. It is generally known that transition metals with high T_m tend to have high ϕ_m [43–45]. In contrast, rare-earth elements tend to exhibit both high T_m and low ϕ_m [46, 34, 47], whereas alkaline earth metals, despite having low T_m, also tend to have low ϕ_m [48, 34]. As a result, many of the final candidates for models (A)–(C) contain one of rare earth and alkaline earth elements. Among these models, in particular model (A), the ETL in contact with the electrode has a relatively large electron affinity, so the allowable upper limit (threshold) of the electrode work function is higher than in the other models. As a result, more materials satisfy this threshold, and the number of candidates that passes the screening criteria is correspondingly larger. Then, to further screen materials, the candidates were arranged in the order of electrical conductivity (accurately, electrical conductivity divided by the relaxation time), as shown in Fig. 8. The electrical conductivity was referenced from Ref. [49], where a large dataset of transport data were obtained by DFT and BoltzTraP calculations assuming a constant relaxation time. Materials without available data were not included in the figure. This figure shows that $ScGa_3$, $CaAl_2$, GdS, and $PrSi_2$ are especially promising among the final candidates for model (A).

Although they are promising from the viewpoints of physical and chemical properties, expensive and air-sensitive characters of these materials possibly make their usage practically difficult.

On the other hand, in model Fig. 1 (D), a relatively large number of candidate materials were obtained. This is because the screening conditions required high T_m and high ϕ_m, leading to the selection of many transition metal compounds. The large number of candidate materials including transition metal compounds suggests that model (D) is promising for practical implementation. Figure 9 shows the electrical conductivity of the candidates. The high rank materials include elemental metals: Cu, W, Fe, and Ni. They are accessible stable materials and therefore promising for practical implementation. Thus, the computational screening workflow proposed in this study is useful for finding out promising electrode materials as well as for selecting versatile device models.

As a final supplementary investigation, we also applied the proposed screening workflow to conventional crystalline Si solar cells. The screened candidates ranked practical materials, such as Al and Ag, among the top candidates, demonstrating the effectiveness of the workflow. Detailed procedures and results are provided in the Supplemental Material.

4. Conclusions

We developed a computational material screening workflow for electrode materials of $BaSi_2$ solar cells. In particular, the accuracy of T_m and ϕ_m estimations was evaluated by comparing conventional methods with machine learning predictions, demonstrating that efficient screening can be performed for a wide variety of materials with machine learning models. Device simulations revealed the thresholds of ϕ_m for four different device models, which were used as one of the screening criteria. Based on the large number of final candidate materials that satisfied the screening conditions, two device configurations were identified as particularly promising for practila implementations: model (A) with 6H-SiC ETL and model (D) with BaS HTL on a metallic electrode. Among the screened candidates, $ScGa_3$, $CaAl_2$, GdS, and $PrSi_2$ were identified as promising electrode materials for model (A) due to their high electrical conductivity, while Cu, W, Fe, and Ni were selected for model (D). Notably, some of these electrode materials have not yet been reported for $BaSi_2$ solar cells. The screening workflow developed in this study is highly versatile and is applicable not only to $BaSi_2$ solar cells but also to other solar cells and semiconductor devices.

Acknowledgment

This work was partly supported by the Murata Science Foundation.

Disclosure statement

The authors report there are no competing interests to declare..

Data availability

The data will be available on request from the corresponding authors.

References

[1] Zhang L, Liu F. High-throughput approach to explore cold metals for electronic and thermoelectric devices. npj Comput Mater. 2024 Apr;10(1). doi:10.1038/s41524-024-01267-w.

[2] Choi HC, Yun H, Yoon JS, et al. Neural approach for modeling and optimizing si-mosfet manufacturing. IEEE Access. 2020;8:159351–159370. doi:10.1109/ACCESS.2020.3019933.

[3] He R, Schierning G, Nielsch K. Thermoelectric devices: A review of devices, architectures, and contact optimization. Adv Mater Technol. 2018;3(4):1700256. doi:10.1002/admt.201700256.

[4] Ferreira-Teixeira S, Pereira AM. Geometrical optimization of a thermoelectric device: Numerical simulations. Energ Convers Manage. 2018;169:217–227. doi:10.1016/j.enconman.2018.05.030.

[5] Omer S, Infield D. Design optimization of thermoelectric devices for solar power generation. Sol Energy Mater Sol Cells. 1998;53(1):67–82. doi:10.1016/S0927-0248(98)00008-7.

[6] Brabec CJ, Sariciftci NS, Hummelen JC. Plastic solar cells. Adv Funct Mater. 2001;11(1):15–26. doi:10.1002/1616-3028(200102)11:1<15::AID-ADFM15>3.0.CO;2-A.

[7] Deepthi Jayan K, Sebastian V. Comprehensive device modelling and performance analysis of $MASnI_3$ based perovskite solar cells with diverse ETM, HTM and back metal contacts. Sol Energy. 2021;217:40–48. doi:10.1016/j.solener.2021.01.058.

[8] Luo S, Li T, Wang X, et al. High-throughput computational materials screening and discovery of optoelectronic semiconductors. WIREs Comput Mol Sci. 2021;11(1):e1489. doi:10.1002/wcms.1489.

[9] Toh K, Saito T, Suemasu T. Optical absorption properties of $BaSi_2$ epitaxial films grown on a transparent silicon-on-insulator substrate using molecular beam epitaxy. Jpn J Appl Phys. 2011;50(6R):068001. doi:10.1143/JJAP.50.068001.

[10] Kumar M, Umezawa N, Imai M. $BaSi_2$ as a promising low-cost, earth-abundant material with large optical activity for thin-film solar cells: A hybrid density functional study. Appl Phys Express. 2014;7(7):071203. doi:10.7567/APEX.7.071203.

[11] Trinh CT, Nakagawa Y, Hara KO, et al. Photoresponse properties of $BaSi_2$ film grown on Si (100) by vacuum evaporation. Mater Res Express. 2016;3(7):076204. doi:10.1088/2053-1591/3/7/076204.

[12] Hara KO, Usami N, Nakamura K, et al. Determination of bulk minority-carrier lifetime in $BaSi_2$ earth-abundant absorber films by utilizing a drastic enhancement of carrier lifetime by post-growth annealing. Appl Phys Express. 2013;6(11):112302. doi:10.7567/APEX.6.112302.

[13] Xu Z, Shohonov DA, Filonov AB, et al. Marked enhancement of the photoresponsivity and minority-carrier lifetime of $BaSi_2$ passivated with atomic hydrogen. Phys Rev Mater. 2019;3(6):065403. doi:10.1103/PhysRevMaterials.3.065403.

[14] Shaalan NM, Hara KO, Trinh CT, et al. Simple method for significant improvement of minority-carrier lifetime of evaporated $BaSi_2$ thin film by sputtered-AlOx passivation. Mater Sci Semicond Process. 2018;76:37–41. doi:10.1016/j.mssp.2017.12.015.

[15] Fujiwara M, Takahashi K, Nakagawa Y, et al. Improved conversion efficiency of p-type $BaSi_2$/n-type crystalline Si heterojunction solar cells by a low growth rate deposition of $BaSi_2$. AIP Adv. 2022 04;12(4):045115. doi:10.1063/5.0083812.

[16] Suemasu T, Morita K, Kobayashi M, et al. Band diagrams of $BaSi_2$/Si structure by Kelvin probe and current–voltage characteristics. Jpn J Appl Phys. 2006;45(6L):L519. doi:10.1143/JJAP.45.L519.

[17] Hara KO. Designing limiting-efficiency $BaSi_2$ solar cells by device simulation and computational material screening. Sol Energy. 2022;245:136–145. doi:10.1016/j.solener.2022.08.044.

[18] Hara KO, Nakanishi T, Ueda R, et al. Inert interlayers and evaporation techniques for high-quality $BaSi_2$ heterostructures. Jpn J Appl Phys. 2025;64(2):02SP31. doi:10.35848/1347-4065/adb167.

[19] Yazaki T, Kunieda S, Arimoto K, et al. Development of flat monoclinic Sm_2O_3 films by sputtering and post-deposition annealing for solar cell applications. Mater Sci Semicond Process. 2025;194:109514. doi:10.1016/j.mssp.2025.109514.

[20] Haku Y, Aonuki S, Yamashita Y, et al. Effect of post-annealing on the significant photoresponsivity enhancement of $BaSi_2$ epitaxial films on Si(111). Appl Phys Express. 2021 jan;14(2):021003. doi:10.35848/1882-0786/abdc9f.

[21] Liu Y, Sun Y, Rockett A. An improved algorithm for solving equations for intra-band tunneling current in heterojunction solar cells. Thin Solid Films. 2012;520(15):4947–4950. doi:10.1016/j.tsf.2012.03.012.

[22] Liu Y, Sun Y, Rockett A. Batch simulation of solar cells by using Matlab and wxAMPS. In: 2012 38th IEEE Photovoltaic Specialists Conference; IEEE; 2012. p. 000902–000905.

[23] Vismara R, Isabella O, Zeman M. Organometallic halide perovskite/barium di-silicide thin-film double-junction solar cells. In: Photonics for Solar Energy Systems VI; Vol. 9898; SPIE; 2016. p. 54–62.

[24] Du W, Baba M, Toko K, et al. Analysis of the electrical properties of Cr/n-$BaSi_2$ Schottky junction and n-$BaSi_2$/p-Si heterojunction diodes for solar cell applications. J Appl Phys. 2014;115(22). doi:10.1063/1.4882117.

[25] Takabe R, Deng T, Kodama K, et al. Impact of Ba to Si deposition rate ratios during molecular beam epitaxy on carrier concentration and spectral response of $BaSi_2$ epitaxial films. J Appl Phys. 2018;123(4). doi:10.1063/1.4994850.

[26] Hara KO. Discovering low-electron-affinity semiconductors for junction partners of photovoltaic $BaSi_2$ by database screening and first principles calculations. J Phys Chem C. 2021;125(44):24310–24317. doi:10.1021/acs.jpcc.1c06338.

[27] Jain A, Ong SP, Hautier G, et al. Commentary: The Materials Project: A materials genome approach to accelerating materials innovation. APL Mater. 2013;1(1):011002.

doi:10.1063/1.4812323.

[28] Ong SP, Richards WD, Jain A, et al. Python Materials Genomics (pymatgen): A robust, open-source python library for materials analysis. Comput Mater Sci. 2013;68:314–319. doi:10.1016/j.commatsci.2012.10.028.

[29] Zur A, McGill TC. Lattice match: An application to heteroepitaxy. J Appl Phys. 1984 01;55(2):378–386. doi:10.1063/1.333084.

[30] Richards WD, Miara LJ, Wang Y, et al. Interface stability in solid-state batteries. Chem Mater. 2016;28(1):266–273. doi:10.1021/acs.chemmater.5b04082.

[31] Li C, Hoe JL, Wu P. Empirical correlation between melting temperature and cohesive energy of binary laves phases. J Phys Chem Solids. 2003;64(2):201–212. doi:10.1016/S0022-3697(02)00267-6.

[32] Kirklin S, Saal JE, Meredig B, et al. The Open Quantum Materials Database (OQMD): assessing the accuracy of DFT formation energies. npj Comput Mater. 2015;1(1):1–15. doi:10.1038/npjcompumats.2015.10.

[33] Hong QJ, Ushakov SV, van de Walle A, et al. Melting temperature prediction using a graph neural network model: From ancient minerals to new materials. Proc Natl Acad Sci. 2022;119(36):e2209630119. doi:10.1073/pnas.2209630119.

[34] Lide DR, editor. CRC handbook of chemistry and physics, internet version 2005. CRC press; 2005. Available from: http://www.hbcpnetbase.com .

[35] Giannozzi P, Baroni S, Bonini N, et al. QUANTUM ESPRESSO: a modular and open-source software project for quantum simulations of materials. J Phys: Condens Matter. 2009;21(39):395502. doi:10.1088/0953-8984/21/39/395502.

[36] Giannozzi P, Andreussi O, Brumme T, et al. Advanced capabilities for materials modelling with Quantum ESPRESSO. J Phys: Condens Matter. 2017;29(46):465901. doi:10.1088/1361-648X/aa8f79.

[37] Sun W, Ceder G. Efficient creation and convergence of surface slabs. Surf Sci. 2013;617:53–59. doi:10.1016/j.susc.2013.05.016.

[38] Perdew JP, Ruzsinszky A, Csonka GI, et al. Restoring the density-gradient expansion for exchange in solids and surfaces. Phys Rev Lett. 2008;100(13):136406. doi:10.1103/PhysRevLett.100.136406.

[39] Schindler P, Antoniuk ER, Cheon G, et al. Discovery of stable surfaces with extreme work functions by high-throughput density functional theory and machine learning. Adv Funct Mater. 2024;34(19):2401764. doi:10.1002/adfm.202401764.

[40] Miedema AR, De Chatel PF, De Boer FR. Cohesion in alloys—fundamentals of a semi-empirical model. Physica B. 1980;100(1):1–28. doi:10.1016/0378-4363(80)90054-6.

[41] Kvålseth TO. Cautionary note about R^2. Amer Statist. 1985;39(4):279–285. doi:10.1080/00031305.1985.10479448.

[42] Kawano H. Effective work functions for ionic and electronic emissions from mono- and polycrystalline surfaces. Prog Surf Sci. 2008;83:1–165. doi:10.1016/j.progsurf.2007.11.001.

[43] Methfessel M, Hennig D, Scheffler M. Trends of the surface relaxations, surface energies, and work functions of the 4d transition metals. Phys Rev B. 1992;46(8):4816. doi:10.1103/PhysRevB.46.4816.

[44] Richter S, Gutschka C, Danner D, et al. High-throughput phase exploration of ternary transition metal carbide TM-X-C (X= Al/Si) thin films. Acta Mater. 2025;288:120839. doi:10.1016/j.actamat.2025.120839.

[45] Tran R, Li XG, Montoya JH, et al. Anisotropic work function of elemental crystals. Surf Sci. 2019;687:48–55. doi:10.1016/j.susc.2019.05.002.

[46] Nikolić MV, Radić SM, Minić V, et al. The dependence of the work function of rare earth metals on their electron structure. Microelectron J. 1996;27(1):93–96. doi:10.1016/0026-2692(95)00097-6.

[47] Mae Y. Schematic interpretation of anomalies in the physical properties of Eu and Yb among the lanthanides. Int J Mater Sci Appl. 2017;6(4):165–170. doi:10.11648/j.ijmsa.20170604.14.

[48] Michaelson HB. The work function of the elements and its periodicity. J Appl Phys. 1977;48(11):4729–4733. doi:10.1063/1.323539.

[49] Ricci F, Chen W, Aydemir U, et al. An ab initio electronic transport database for inorganic materials. Scientific data. 2017;4(1):1–13. doi:10.1038/sdata.2017.85.

[50] Migas DB, Shaposhnikov VL, Borisenko VE. Isostructural $BaSi_2$, $BaGe_2$ and $SrGe_2$: electronic and optical properties. Phys Status Solidi B. 2007;244(7):2611–2618. doi:10.1002/pssb.200642556.

[51] Chang IYK, Hwang YR, Juan PC, et al. Temperature dependence of the current conduction mechanisms in Sm_2O_3 thin films. J Electrochem Soc. 2008 oct;155(12):G265. doi:10.1149/1.2979141.

[52] Zollner S, Chen JG, Duda E, et al. Dielectric functions of bulk 4H and 6H SiC and spectroscopic ellipsometry studies of thin SiC films on Si. J Appl Phys. 1999;85(12):8353–8361. doi:10.1063/1.370682.

[53] Kaneko Y, Koda T. New developments in IIa–VIb (alkaline-earth chalcogenide) binary semiconductors. J Cryst Growth. 1988;86(1-4):72–78. doi:10.1016/0022-0248(90)90701-L.

[54] Stewart AD, Gerger A, Gila BP, et al. Determination of Sm_2O_3/GaAs heterojunction band offsets by x-ray photoelectron spectroscopy. Appl Phys Lett. 2008;92(15):153511. doi:10.1063/1.2911726.

[55] Gobeli GW, Allen FG. Photoelectric properties of cleaved GaAs, GaSb, InAs, and InSb surfaces; comparison with Si and Ge. Phys Rev. 1965;137(1A):A245.

doi:10.1103/PhysRev.137.A245.

[56] Davydov SY. On the electron affinity of silicon carbide polytypes. Semiconductors. 2007;41:696–698. doi:10.1134/S1063782607060152.

[57] Hu CY, Hensley EB. Electron affinities of the barium chalcogenides. J Appl Phys. 1969;40(8):3346–3351. doi:10.1063/1.1658186.

Figure 1. Device models used for simulations.

Figure 2. The calculated band alignments of the model (C) in Fig. 1 with PBH = (a) 0.0 and (b) 0.5 eV under dark conditions. Upper blue line denotes the conduction band minimum while the lower orange line denotes the valence band maximum.

Figure 3. (a)–(d) Simulated PCE of solar cells as functions of the ϕ_m of metallic electrodes in models (A)–(D), where the electrodes are in contact with 6H-SiC, 4H-SiC, Sm_2O_3, and BaS, respectively. The red dashed line indicates a PCE of 30%. The insets show the band alignments near the back electrode for specific work functions. CB and VB denote the conduction and valence bands, respectively.

Figure 4. Workflow of computational material screening for metallic electrodes of solar cells proposed in this study.

Figure 5. T_m plotted against E_{coh} of randomly selected binary metallic compounds, along with the regression line.

Figure 6. Comparison of the T_m of binary metallic compounds estimated by the linear regression (circles) and the machine learning model [33] (squares) with the reference values.

Figure 7. Comparison of the ϕ_m of elemental metals estimated by DFT and the machine learning model [39]. The surface orientation selected was (100) for all data.

Figure 8. Electrical conductivity of the candidate materials for model (A). The electrical conductivity divided by the relaxation time is shown.

Figure 9. Electrical conductivity of the candidate materials for model (D). The electrical conductivity divided by the relaxation time is shown.

Table 1. Material properties used for device simulations.

	Material				
Parameter	$BaSi_2$	BaS	Sm_2O_3	6H-SiC	4H-SiC
Dielectric constant	14 [50]	15 [27]	15 [51]	8 [52]	8 [52]
E_g (eV)	1.3 [9, 10, 11]	3.81 [53]	5.16 [54, 55]	3.0 [56]	3.2 [56]
Electron affinity (eV)	3.2 [16]	0.84 [57]	2.94 [54, 55]	3.5 [56]	3.2 [56]

Formula	T_m (K)	ϕ_m (eV)	Formula	T_m (K)	ϕ_m (eV)	Formula	T_m (K)	ϕ_m (eV)
Ba_3Ge_4	1423	3.67	EuSi	1597	3.73	PrS	2478	2.60
Ba_3Ge_5	1418	3.48	$EuSi_2$	1756	3.73	PrSb	2384	3.30
Ba_3Si_4	1412	3.90	EuSn	1373	3.53	PrSi	1934	3.69
Ba_5Sb_3	1405	2.90	$GdAl_2$	1774	3.69	$PrSi_2$	1942	3.56
$BaAl_4$	1325	3.50	$GdAl_3$	1761	3.70	$PrSn_2$	1437	3.55
$BaGa_2$	1290	3.08	$GdGa_2$	1635	3.54	$PrSn_3$	1434	3.33
$BaGa_4$	1277	3.56	$GdGa_3$	1642	3.78	$ScAl_3$	1654	3.82
BaGe	1426	3.41	GdGe	2041	3.52	$ScGa_3$	1393	3.73
BaSi	1413	3.38	GdN	2994	3.23	ScGe	2276	3.82
BaSn	1416	3.29	GdP	2996	3.52	ScN	2747	3.44
$Ca_{11}Sb_{10}$	1310	3.50	GdS	2530	2.87	ScP	2569	3.75
$CaAl_2$	1342	3.70	GdSb	2421	3.51	ScSb	2488	3.70
$CaGa_2$	1277	3.79	GdSi	2091	3.81	ScSi	2259	3.86
CaGe	1432	3.83	$GdSn_2$	1396	3.62	$Sm_{11}Sn_{10}$	1758	3.43
$CaGe_2$	1308	3.85	Ho_3Ge_4	2089	3.75	Sm_3Ge_5	1743	3.75
CaSi	1524	3.67	Ho_3Ge_5	1788	3.84	$SmAl_3$	1737	3.70
CaSn	1374	3.25	Ho_3Sn_7	1362	3.82	$SmGa_2$	1640	3.47
Ce_3Al_{11}	1530	3.76	$HoAl_3$	1763	3.82	$SmGa_3$	1646	3.76
Ce_3Ge_5	1755	3.78	$HoGa_2$	1583	3.57	SmGe	1790	3.56
Ce_3Sn_7	1434	3.74	$HoGa_3$	1596	3.84	SmS	2288	3.80
Ce_4Ge_7	1752	3.67	HoGe	2161	3.73	SmSi	2064	3.44
Ce_4H_{11}	1333	3.66	HoP	2713	3.60	$SmSn_2$	1373	3.58
Ce_7O_{12}	2587	3.77	HoS	2550	3.07	$SmSn_3$	1381	3.40
$CeAl_3$	1591	3.85	HoSb	2398	3.59	Sr_5Sb_3	1309	3.27
$CeGa_3$	1707	3.73	HoSi	2132	3.71	$SrAl_4$	1327	3.51
$CeGa_6$	1591	3.87	$HoSn_2$	1357	3.85	$SrGa_2$	1283	3.27
CeN	3025	2.97	La_2H_5	1320	3.42	$SrGa_4$	1276	3.63
CeP	2986	3.31	La_2H_5	1320	3.58	SrGe	1426	3.58
CeS	2652	2.65	La_2Sn_3	1445	3.46	$SrGe_2$	1405	3.71
CeSb	2073	3.29	La_3Al_{11}	1524	3.82	SrSi	1421	3.85
$CeSb_2$	1829	3.89	La_3Ge_5	1748	3.66	SrSn	1394	3.49
$CeSn_3$	1433	3.33	La_3Sn_7	1436	3.58	Tb_3Ge_4	2059	3.61
Dy_3Ge_4	2095	3.69	$LaGa_2$	1725	3.34	Tb_3Ge_5	1888	3.76
Dy_3Ge_5	1868	3.75	LaGe	1758	3.25	Tb_3Sn_7	1374	3.78
Dy_5S_7	1944	3.86	LaP	2727	3.27	Tb_5S_7	1963	3.81
Dy_5Sn_{11}	1358	3.80	LaS	2429	2.47	$TbAl_3$	1762	3.71

$DyAl_3$	1760	3.72	LaSb	2051	3.29	$TbGa_2$	1573	3.55
$DyGa_2$	1589	3.57	$LaSb_2$	1801	3.86	$TbGa_3$	1551	3.72
$DyGa_3$	1608	3.74	$LaSn_3$	1433	3.27	TbGe	2137	3.68
DyGe	2138	3.36	$Lu_{11}Ge_{10}$	2253	3.65	TbS	2602	3.90
DyP	2690	3.60	Lu_3Ge_4	2107	3.88	TbSi	2107	3.41
DyS	2557	3.01	$LuAl_3$	1741	3.73	$TbSn_2$	1372	3.69
DySb	2383	3.58	$LuGa_2$	1572	3.80	TiF_3	1707	3.55
DySi	2119	3.86	$LuGa_3$	1530	3.67	TiN	3225	3.55
Er_3Ge_4	2162	3.75	$LuGe_2$	1574	3.85	Tm_3Ge_4	2125	3.82
Er_3Sn_7	1351	3.83	LuP	2534	3.62	$TmAl_3$	1758	3.79
$ErAl_3$	1758	3.65	LuSb	2394	3.61	$TmGa_2$	1573	3.76
$ErGa_2$	1578	3.61	$LuSn_2$	1335	3.87	$TmGa_3$	1565	3.81
$ErGa_3$	1584	3.79	Nd_2Sn_3	1437	3.52	TmGe	2211	3.75
ErGe	2211	3.84	Nd_3Ge_5	1802	3.74	TmP	2636	3.64
ErP	2595	3.62	Nd_3Sn_7	1430	3.63	TmSi	2139	3.83
ErS	2394	3.10	$NdAl_3$	1721	3.63	$TmSn_2$	1334	3.74
ErSb	2348	3.60	$NdGa_2$	1732	3.39	Y_3Ge_4	2146	3.60
ErSi	2141	3.85	$NdGa_3$	1716	3.75	Y_3Ge_5	1928	3.77
$ErSn_2$	1346	3.83	NdGe	1797	3.50	YAl_3	1754	3.66
$Eu_{16}Sb_{11}$	1811	3.49	NdP	2842	3.36	YGa_2	1630	3.56
Eu_3Ge_5	1330	3.61	NdS	2525	2.64	YGa_3	1631	3.80
Eu_3P_4	1609	3.89	NdSb	2384	3.29	YGe	2193	3.71
Eu_5Sb_3	1791	3.24	NdSi	1941	3.59	YP	2697	3.59
$EuAl_4$	1366	3.64	$NdSn_2$	1433	3.54	YSi	2124	3.79
$EuGa_2$	1292	3.51	$NdSn_3$	1428	3.35	YSn_2	1356	3.85
$EuGa_4$	1286	3.77	Pr_2Sn_3	1440	3.50	Zr_5Zn_{39}	1303	3.81
EuGe	1423	3.56	$PrAl_3$	1659	3.85	$ZrAl_3$	1860	3.81
EuO	2246	3.03	$PrGa_2$	1736	3.37	ZrC	3534	3.85
EuP	2256	3.38	$PrGa_3$	1725	3.73	$ZrGa_3$	1650	3.90
EuS	2534	2.85	PrGe	1768	3.50			

Table 2.: List of candidate metallic materials for model (A): 6H-SiC contacting layer. The estimated T_m and ϕ_m are also summarized.

Formula	T_m (K)	ϕ_m (eV)	Formula	T_m (K)	ϕ_m (eV)	Formula	T_m (K)	ϕ_m (eV)
Ba_3Ge_5	1418	3.48	EuS	2534	2.85	$NdSn_2$	1433	3.54
Ba_5Sb_3	1405	2.90	EuSn	1373	3.53	$NdSn_3$	1428	3.35

$BaAl_4$	1325	3.50	$GdGa_2$	1635	3.54	Pr_2Sn_3	1440	3.50
$BaGa_2$	1290	3.08	GdGe	2041	3.52	$PrGa_2$	1736	3.37
$BaGa_4$	1277	3.56	GdN	2994	3.23	PrGe	1768	3.50
BaGe	1426	3.41	GdP	2996	3.52	PrS	2478	2.60
BaSi	1413	3.38	GdS	2530	2.87	PrSb	2384	3.30
BaSn	1416	3.29	GdSb	2421	3.51	$PrSi_2$	1942	3.56
$Ca_{11}Sb_{10}$	1310	3.5	$HoGa_2$	1583	3.57	$PrSn_2$	1437	3.55
CaSn	1374	3.25	HoP	2713	3.60	$PrSn_3$	1434	3.33
CeN	3025	2.97	HoS	2550	3.07	ScN	2747	3.44
CeP	2986	3.31	HoSb	2398	3.59	$Sm_{11}Sn_{10}$	1758	3.43
CeS	2652	2.65	La_2H_5	1320	3.42	$SmGa_2$	1640	3.47
CeSb	2073	3.29	La_2H_5	1320	3.58	SmGe	1790	3.56
$CeSn_3$	1433	3.33	La_2Sn_3	1445	3.46	SmSi	2064	3.44
$DyGa_2$	1589	3.57	La_3Sn_7	1436	3.58	$SmSn_2$	1373	3.58
DyGe	2138	3.36	$LaGa_2$	1725	3.34	$SmSn_3$	1381	3.40
DyP	2690	3.60	LaGe	1758	3.25	Sr_5Sb_3	1309	3.27
DyS	2557	3.01	LaP	2727	3.27	$SrAl_4$	1327	3.51
DySb	2383	3.58	LaS	2429	2.47	$SrGa_2$	1283	3.27
$ErGa_2$	1578	3.61	LaSb	2051	3.29	SrGe	1426	3.58
ErS	2394	3.10	$LaSn_3$	1433	3.27	SrSn	1394	3.49
ErSb	2348	3.60	LuSb	2394	3.61	$TbGa_2$	1573	3.55
$Eu_{16}Sb_{11}$	1811	3.49	Nd_2Sn_3	1437	3.52	TbSi	2107	3.41
Eu_3Ge_5	1330	3.61	$NdGa_2$	1732	3.39	TiF_3	1707	3.55
Eu_5Sb_3	1791	3.24	NdGe	1797	3.50	TiN	3225	3.55
$EuGa_2$	1292	3.51	NdP	2842	3.36	Y_3Ge_4	2146	3.60
EuGe	1423	3.56	NdS	2525	2.64	YGa_2	1630	3.56
EuO	2246	3.03	NdSb	2384	3.29	YP	2697	3.59
EuP	2256	3.38	NdSi	1941	3.59			

Table 3.: List of candidate metallic materials for model (B): 4H-SiC contacting layer. The estimated T_m and ϕ_m are also summarized.

Formula	T_m (K)	ϕ_m (eV)	Formula	T_m (K)	ϕ_m (eV)	Formula	T_m (K)	ϕ_m (eV)
Ba_2Ge	1431	2.75	Eu_5Sb_3	1791	3.24	Pr_5Sb_3	1999	3.11
Ba_2Si	1409	3.02	EuO	2246	3.03	Pr_5Sn_3	1772	3.21
Ba_2Sn	1457	2.88	EuS	2534	2.85	PrAl	1714	3.17
Ba_5Sb_3	1405	2.90	Gd_2C	2451	3.20	PrS	2478	2.60
$BaGa_2$	1290	3.08	GdN	2994	3.23	PrSb	2384	3.30
BaSn	1416	3.29	LaS	2429	2.47	Sm	1352	2.91

CaSn	1374	3.25	LaSb	2051	3.29	Sm_2C	1708	3.16
Ce_2C_3	2547	3.29	$LaSn_3$	1433	3.27	Sm_5Ge_3	1886	3.17
CeN	3025	2.97	Nd_3Ga_2	1523	3.28	Sm_5Sb_3	1997	3.31
CeO	2365	2.90	Nd_5Ge_3	1911	3.27	Sm_5Si_3	1892	3.32
CeP	2986	3.31	Nd_5Si_4	1935	3.18	Sm_5Sn_3	1774	3.27
Eu_2Ge	1521	3.27	Nd_5Sn_3	1816	3.22	Sr_5Sb_3	1309	3.27
Eu_2Si	1513	3.17	NdAl	1633	3.24	$SrGa_2$	1283	3.27
Eu_2Sn	1623	3.13	NdSb	2384	3.29			

Table 4.: List of candidate metallic materials for model (C): Sm_2O_3 contacting layer.The estimated T_m and ϕ_m are also summarized.

Formula	T_m (K)	ϕ_m (eV)	Formula	T_m (K)	ϕ_m (eV)	Formula	T_m (K)	ϕ_m (eV)
$Al_{13}Fe_4$	1434	4.28	$GaNi_3$	1658	4.63	NiSb	1437	4.36
Al_3Cr	1762	4.32	GdB_4	2836	4.41	P_2W	1965	4.76
Al_3Ni_2	1885	4.32	GdH_2	1284	4.59	PW	2702	4.70
Al_3Ni_5	1840	4.44	Ge_2Mo	1815	4.51	PrB_4	2842	4.34
Al_4Cu_9	1327	4.26	$GeMo_3$	2453	4.43	PrH_2	1339	4.50
Al_4Ni_3	1899	4.40	Hf_3N_2	3447	4.51	RbC_8	2915	5.04
Al_5Co_2	1493	4.26	HfB_2	3489	4.43	$Sc_{39}N_{34}$	2770	4.72
Al_5W	1983	4.24	HfH_2	2487	4.41	Si_2Mo	2263	4.44
AlCo	1899	4.36	HfP	2893	4.41	Si_2Ni	1600	4.74
$AlFe_3$	1749	4.48	HfP_2	1935	4.61	Si_2W	2435	4.55
$AlMo_3$	2077	4.25	HfS	2660	4.68	Si_3Mo_5	2437	4.27
AlNi	1900	4.48	HoB_4	2737	4.45	$SiMo_3$	2464	4.52
$AlNi_3$	1627	4.58	HoH_2	1354	4.60	SiNi	1390	4.69
$B_{13}C_2$	2683	5.33	KC_8	3028	5.03	$SiNi_2$	1617	4.53
B_2Mo	2707	4.65	LaB_4	2349	4.28	$SiNi_3$	1677	4.71
B_2W	2738	5.06	LaH_2	1332	4.48	SmB_4	2800	4.39
BMo	2843	4.56	LuB_4	2694	4.52	SmH_2	1344	4.53
BW	3023	4.43	Mn	1537	4.29	SmN	2817	4.30
BW_2	3011	4.54	$Mn_{23}C_6$	1841	4.32	SmP	2431	4.27
BaC_6	2696	4.91	$Mn_{29}H_2$	1351	4.36	Ta_2C	3577	4.82
Ce_2O_3	2484	5.48	Mn_2N	1703	4.50	Ta_2N	3291	4.48
CeB_4	2368	4.43	Mn_2P	1553	4.42	Ta_3B_2	2899	4.25
CeB_6	2541	4.82	Mn_2P	1553	4.39	Ta_3B_4	3315	4.45
Co	1767	4.86	Mn_3Co	1364	4.33	Ta_3S_2	2491	4.26
Co_2P	1654	4.57	Mn_3Co	1364	4.38	Ta_5S_8	2198	4.57

Co_2Si	1648	4.50	Mn_4N	1653	4.58	Ta_5S_8	2198	4.61
Co_3Ni	1467	4.53	MnAl	1474	4.35	Ta_7S_{12}	2182	4.37
Co_3S_4	1561	5.02	$MnAl_{12}$	1354	4.25	TaB	3055	4.40
Co_9S_8	1455	4.84	$MnAl_6$	1401	4.26	TaB_2	3360	4.61
CoB	1735	4.91	MnB	2157	4.62	$TaCo_3$	1837	4.45
CoGe	1490	4.48	MnB_4	2401	5.04	TaH_2	2125	5.08
CoH	1288	4.70	MnCo	1618	4.34	TaN	3282	4.62
CoP	1456	4.96	MnGa	1361	4.46	$TaNi_3$	1764	4.40
CoSi	1733	4.60	$MnNi_3$	1533	4.63	TaP	2282	4.25
$CoSi_2$	1661	4.74	MnP	1440	4.65	$TaSi_2$	2264	4.26
CoSn	1498	4.43	MnS_2	1441	5.05	TbB_4	2759	4.43
Cr_2O_3	2521	5.05	MnV	1677	4.25	TbH_2	1427	4.58
Cr_3C_2	2130	4.42	$Mo_{15}N_{16}$	2333	4.85	TbH_3	1286	5.22
Cr_3Si	2030	4.47	$Mo_{15}N_{16}$	2333	4.75	TbP	2705	4.34
Cr_7C_3	2065	4.35	Mo_2C	2785	4.32	Ti_2C	2514	4.26
CrB_4	2434	4.82	MoN	2329	4.99	Ti_2O	2203	4.53
CrP	1882	4.48	MoP	2139	4.64	Ti_8C_5	2974	4.39
$CrSi_2$	1756	4.42	MoP_2	1600	4.56	TiB	2598	4.33
CsC_8	2774	5.46	MoW	2880	4.40	TiB_2	3301	4.31
Cu	1340	4.52	Nb_2B_3	3273	4.56	TiO	2136	4.50
DyB_4	2752	4.42	Nb_2N	2307	4.51	TiP	2382	4.32
DyH_2	1376	4.62	Nb_3B_4	3183	4.33	TiS	2282	4.37
ErB_4	2679	4.43	Nb_3S_4	1937	4.46	TmB_4	2666	4.47
ErH_2	1313	4.59	Nb_3S_5	1949	4.39	TmH_2	1352	4.60
EuH_2	1292	4.32	Nb_5N_6	2440	4.30	V_2B_3	2767	4.57
Fe	1784	4.55	NbB_2	3293	4.49	V_2N	2264	4.68
Fe_2B	1576	4.77	$NbCo_3$	1726	4.25	V_2O_3	2118	6.07
Fe_2P	1642	4.54	NbH_2	1867	5.12	V_3B_4	2718	4.38
Fe_2W	1954	4.39	NbN	2439	5.62	V_3S_4	2027	4.40
Fe_3Co	1449	4.64	NbP_2	1839	4.41	V_3Si	2198	4.31
Fe_3Ge	1470	4.62	NdB_4	2850	4.37	V_5B_6	2641	4.40
Fe_3N	1861	4.92	NdH_2	1337	4.52	VB	2522	4.41
Fe_3P	1646	4.51	NdH_3	1322	4.67	VB_2	2830	4.59
Fe_3Si	1643	4.67	Ni	1752	4.79	VFe_3	1723	4.36
Fe_3Sn_2	1489	4.41	$Ni_{12}P_5$	1466	4.62	VN	2481	4.79
Fe_9Co_7	1699	4.47	$Ni_{19}Ge_{12}$	1449	4.47	VNi_3	1643	4.36
FeB	1897	4.92	Ni_2B	1678	4.81	VSi_2	1924	4.26
FeCo	1700	4.51	Ni_3B	1471	4.50	VW	2931	4.28
FeGe	1385	4.56	Ni_3Ge	1723	4.63	W	3526	4.48

FeH	1481	4.67	Ni_3Mo	1684	4.39	W_2N_3	2902	4.99
FeN	1848	5.80	Ni_3P	1506	4.58	WC	2964	4.94
FeNi	1553	4.72	Ni_3S_2	1359	4.95	YB_4	2951	4.45
$FeNi_3$	1498	4.83	Ni_3Sn	1434	4.61	Zn_3N_2	1579	4.41
FeP	1430	4.97	Ni_3Sn_2	1500	4.39	ZnNi	1346	4.48
FeS	1452	4.77	Ni_3Sn_4	1285	4.36	ZrB_2	3325	4.24
FeSn	1388	4.42	Ni_4B_3	1499	4.82	ZrH_2	1910	4.28
$Ga_{31}Mo_6$	1355	4.26	Ni_4Sn_3	1501	4.41	ZrN	3252	4.44
Ga_3Ni_2	1509	4.36	Ni_4W	1766	4.31	ZrP	2537	4.30
Ga_3Ni_5	1504	4.44	Ni_5Ge_3	1450	4.48	ZrP_2	1764	4.51
Ga_9Ni_{13}	1505	4.35	Ni_5P_4	1361	4.68	ZrS	2436	4.62
GaCo	1497	4.42	Ni_9S_8	1331	4.71	ZrSi	2507	4.24
$GaFe_3$	1667	4.67	NiGe	1446	4.54	$ZrSi_2$	2200	4.33
$GaMo_3$	2461	4.30	NiH	1276	4.64			

Table 5.: List of candidate metallic materials for model (D): BaS contacting layer.The estimated T_m and ϕ_m are also summarized.

SUPPLEMENTAL MATERIAL

Computational material screening for electrode materials of $BaSi_2$ solar cells

Tomoaki Yazaki[a], Keisuke Arimoto[a], Junji Yamanaka[a], and Kosuke O. Hara[b]

[a]University of Yamanashi, 7-32 Miyamae, Kofu, Yamanashi, Japan

[b]Nara Institute of Science and Technology, 8916-5 Takasyama, Ikoma, 630-0192, Nara, Japan

1. Data list of work functions

Table S1 lists the work functions of elemental metals estimated by the density functional theory (DFT) calculations and the machine learning model [S1] together with reference values [S2].

Table S1 Work functions of elemental metals estimated by DFT calculations and the machine learning model [S1] together with reference values [S2]. Estimations are for (100) orientations. Reference values are for (100) if available; otherwise, for polycrystalline samples.

Formula	Work function (DFT) [eV]	Work function (machine learning) [eV]	Work function (reference [S2]) [eV]
Ag	4.39	4.22	4.64
Al	4.38	4.25	4.2
Au	5.23	4.90	5.47
Ba	2.40	2.33	2.52
Be	3.93	3.86	4.98
Ca	2.76	2.79	2.87
Cs	1.99	2.01	1.95
Cu	4.65	4.61	5.1
Ga	4.37	4.33	4.32
Hf	3.69	3.57	3.9

In	3.95	4.01	4.09
K	2.22	2.38	2.29
Li	3.06	3.01	2.93
Mg	3.69	3.51	3.66
Mo	3.98	4.00	4.53
Na	2.66	2.83	2.36
Nb	3.67	3.75	4.02
Os	4.89	4.81	5.93
Pb	3.85	3.94	4.25
Pd	5.23	5.03	5.22
Pt	5.81	5.59	5.64
Rb	2.17	2.21	2.261
Re	4.52	4.42	4.72
Rh	5.23	4.96	4.98
Ru	4.60	4.44	4.71
Sc	3.32	3.23	3.5
Sn	4.27	4.29	4.42
Ta	3.90	4.22	4.15
Ti	3.70	3.49	4.33
V	3.84	4.00	4.3
W	4.21	4.36	4.63
Zn	4.60	4.07	3.63
Zr	3.68	3.41	4.05

2. Validation of the screening workflow on pn-junction Si solar cells

To validate our screening workflow, we searched for electrode materials for pn-junction crystalline Si solar cells. The device model for simulations consisted of an n-type Si layer (100 nm) on the top side and a p-type Si layer (200 μm) on the bottom side. The electron and hole concentrations in the n- and p-type layers were 1×10^{19} cm^{-3} and 1×10^{16} cm^{-3}, respectively. The permittivity, bandgap, electron affinity, effective density of states of the conduction band, effective density of states of the valence band, electron mobility, and hole mobility were 11.9, 1.12 eV, 4.05 eV, 2.86×10^{19} cm^{-3}, 2.66×10^{19} cm^{-3}, 1450 $cm^2/V\cdot s$, and 505 $cm^2/V\cdot s$, respectively, according to ref. [S3]. The optical absorption coefficients were taken from ref. [S4]. Because wxAMPS does not accept Auger recombination coefficients, acceptor-type midgap defects

were assumed to simulate realistic Si materials. We assumed the density, energy level, and capture cross section to be 1×10^{12} cm^{-3}, 0.56 eV, and 1×10^{-16} cm^2, respectively. This led to a carrier lifetime of approximately 1 ms. The simulation temperature was 300 K, and the effective surface recombination speed was 1×10^{7} cm/s. The top and bottom reflectances were 0 and 1, respectively.

Figure S1 shows the power conversion efficiency of the pn-junction Si solar cells as functions of the work functions of the bottom and top electrodes. These results indicate the range of work functions that yield high power conversion efficiency: Specifically, $\geq$ 5.45 eV for the bottom electrode and $\leq$ 3.65 eV for the top electrode.

Then, computational material screening was performed. For the validation, the search space was confined to elements excluding noble gases, radioactive elements, and actinoids. The melting point threshold was set to 300 K. Table S2 summarizes the candidate materials in descending order of electrical conductivity (accurately, electrical conductivity divided by the relaxation time. Please see the main text for details). Work function criteria were not considered to prepare this table. If we apply the work function criteria, only Na remains as a candidate. However, Na is highly reactive with air and is therefore not used in practical solar cells. Additionally, a common approach is to heavily dope with impurities to avoid the effect of Fermi level pinning and form ohmic contacts on Si by taking advantage of its excellent dopability. Therefore, ignoring the work function criterion aligns with the design concept of practical Si solar cells. However, if we consider other semiconductors that do not significantly suffer from Fermi level pinning, the work function criteria would be useful for effective screening. Table S2 shows that Al, In, Ag, etc. are promising candidates. This result agrees with the electrode materials (Al and Ag) used in practical Si solar cells [S5]. In is avoided probably because of its low melting point, scarcity of resources, and high cost. Thus, our screening workflow has been shown to reach practical electrode materials for crystalline Si solar cells.

Figure S1 Power conversion efficiency of pn-junction solar cells simulated by wxAMPS as functions of work function of (a) bottom and (b) top electrodes.

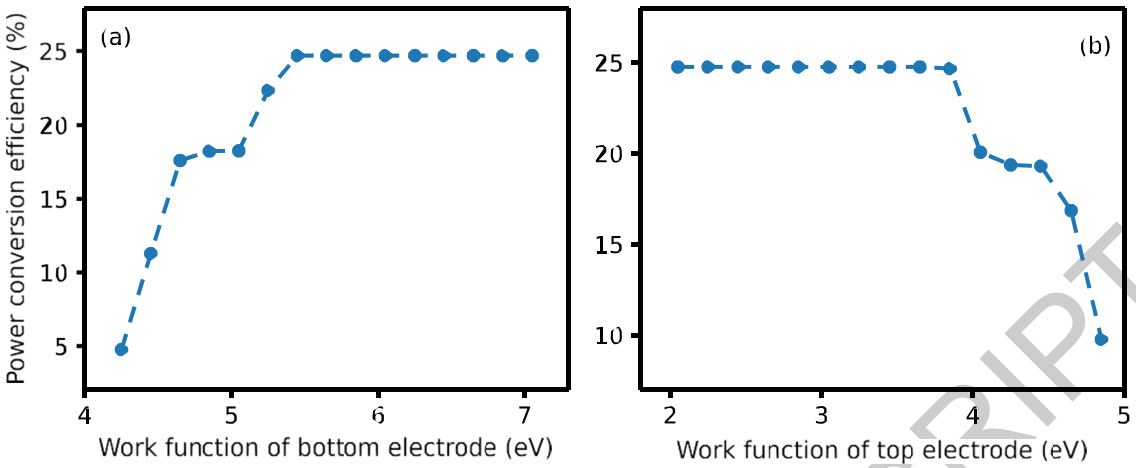

Table S2 List of elements that passed computational material screening. The considered criteria included bandgap, phase stability, interface reactivity, and melting point. The estimated work function is also listed, but was not used for screening. The elements are listed in descending order of electrical conductivity divided by the relaxation time.

Formula	mp-ID	Melting point (K)	Work function (eV)	Electrical conductivity (S/cm·s)
Al	mp-134	991	4.19	3.13×10^{6}
In	mp-85	404	4.05	1.99×10^{6}
Ag	mp-8566	1208	4.19	1.66×10^{6}
Zn	mp-79	647	4.03	1.65×10^{6}
Pb	mp-20483	566	3.96	1.64×10^{6}
Au	mp-81	1277	4.87	1.56×10^{6}
Cd	mp-94	617	3.93	1.23×10^{6}
Tl	mp-82	562	3.81	1.04×10^{6}
Na	mp-10172	350	2.80	7.29×10^{5}
Be	mp-87	1542	4.46	7.22×10^{5}
Ga	mp-142	314	4.29	5.40×10^{5}
Sb	mp-104	853	4.70	2.82×10^{4}
Sn	mp-117	503	4.29	2.71×10^{4}
Ge	mp-32	1176	4.74	1.76×10^{3}

References

[S1] Schindler P, Antoniuk ER, Cheon G, et al. Discovery of stable surfaces with extreme work functions by high-throughput density functional theory and machine learning. Adv Funct Mater. 2024;34(19): 2401764.

[S2] Lide DR, editor. CRC handbook of chemistry and physics, internet version 2005. CRC press; 2005. [S3] Sze SM., Semiconductor Devices: Physics and Technology, 2nd Edition. John Wiley & Sons. Inc.; 2002, translated by YNannichi Y, Kawabe M, and Hasegawa F, Japan UNI Agency, Inc.; 2004.
[S4] Green MA and Keevers M, Optical properties of intrinsic silicon at 300 K, Prog Photovolt. 1995;3:189.
[S5] Avrutin V, Izyumskaya N, and Morkoç H, Semiconductor solar cells: Recent progress in terrestrial applications. Superlattices Microstruct. 2011;49:337.

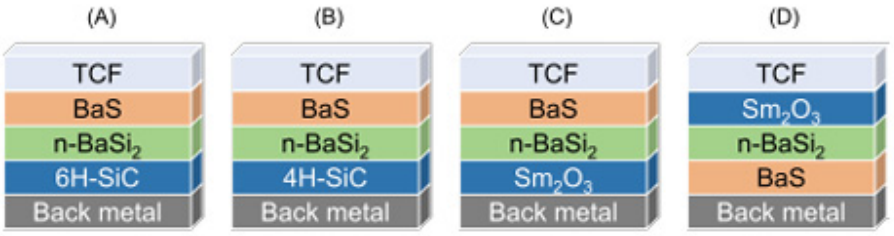

Figure 1. Device models used for simulations.

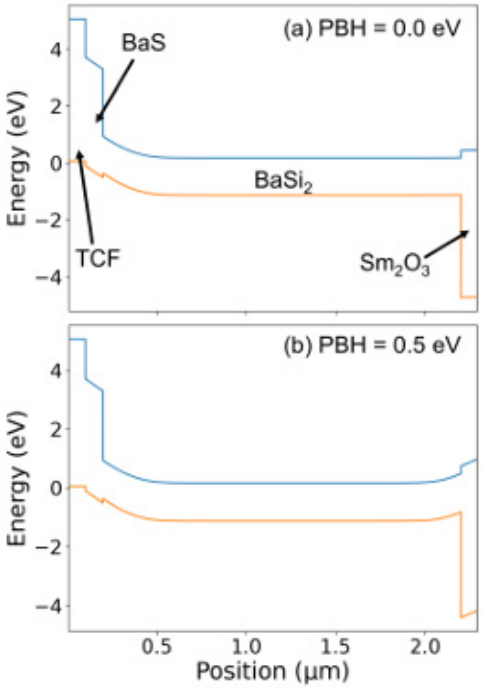

Figure 2. The calculated band alignments of the model (C) in Fig. 1 with PBH = (a) 0.0 and (b) 0.5 eV under dark conditions. Upper blue line denotes the conduction band minimum while the lower orange line denotes the valence band maximum.

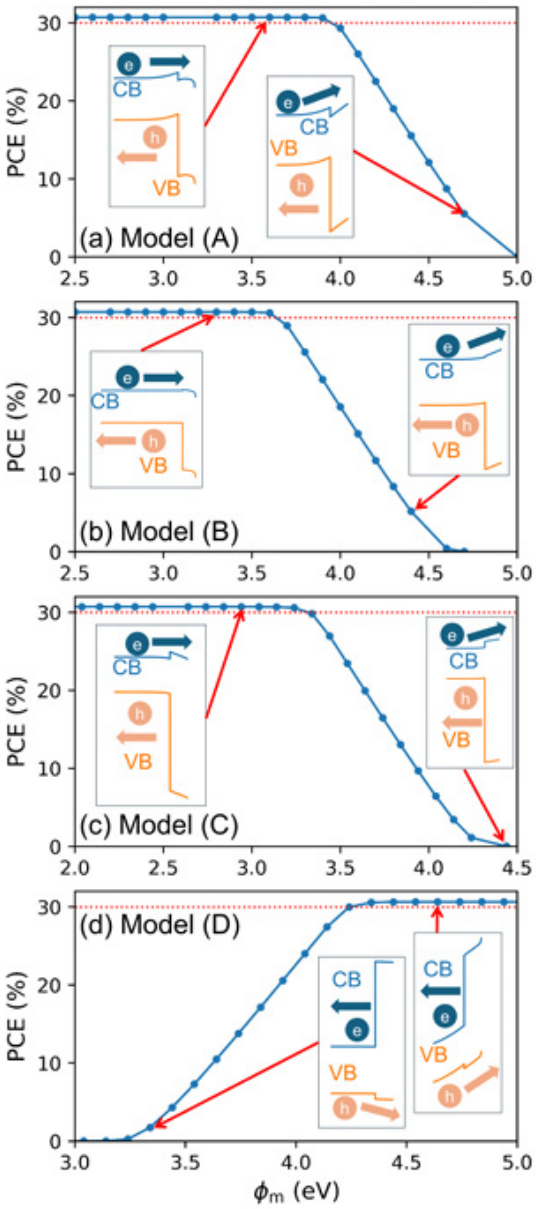

Figure 3. (a)–(d) Simulated PCE of solar cells as functions of the ϕ_m of metallic electrodes in models (A)–(D), where the electrodes are in contact with 6H-SiC, 4H-SiC, Sm_2O_3, and BaS, respectively. The red dashed line indicates a PCE of 30%. The insets show the band alignments near the back electrode for specific work functions. CB and VB denote the conduction and valence bands, respectively.

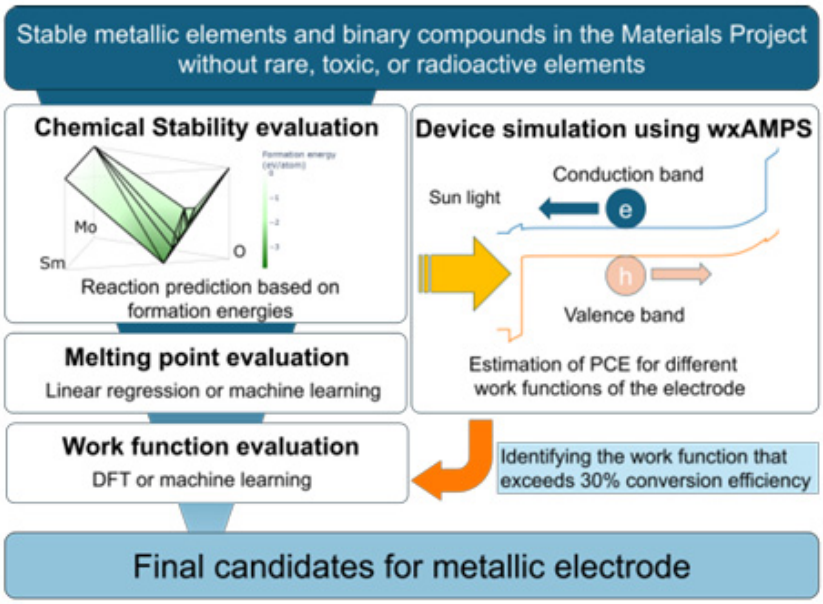

Figure 4. Workflow of computational material screening for metallic electrodes of solar cells proposed in this study.

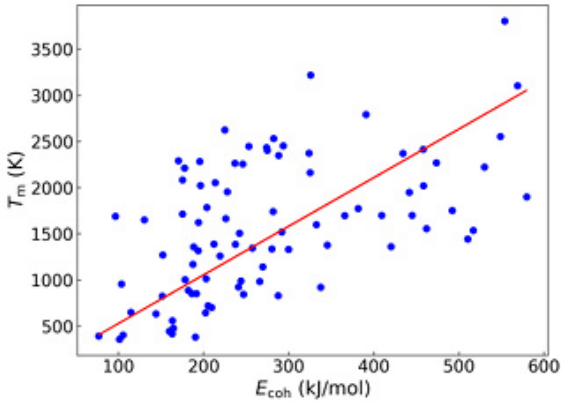

Figure 5. T_m plotted against E_{coh} of randomly selected binary metallic compounds, along with the regression line.

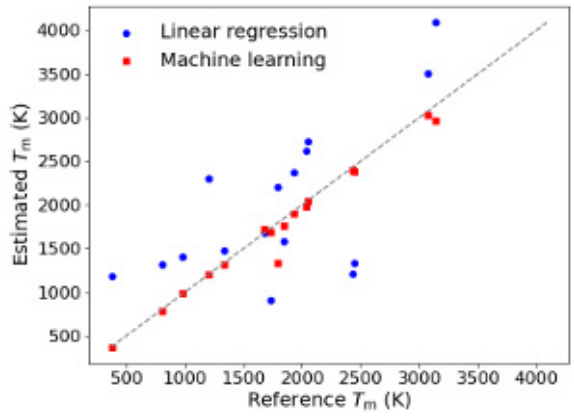

Figure 6. Comparison of the T_m of binary metallic compounds estimated by the linear regression (circles) and the machine learning model [33] (squares) with the reference values.

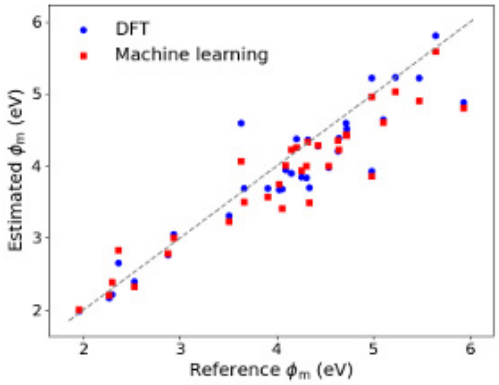

Figure 7. Comparison of the ϕ_m of elemental metals estimated by DFT and the machine learning model [39]. The surface orientation selected was (100) for all data.

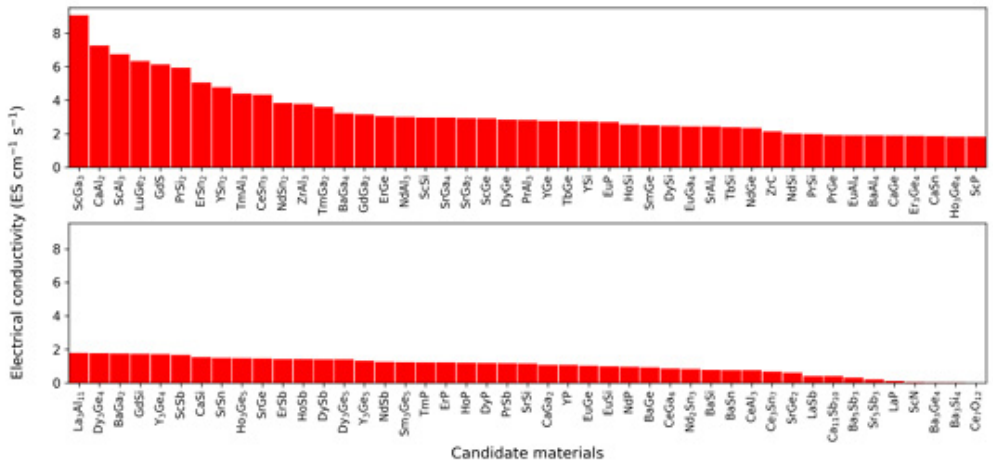

Figure 8. Electrical conductivity of the candidate materials for model (A). The electrical conductivity divided by the relaxation time is shown.

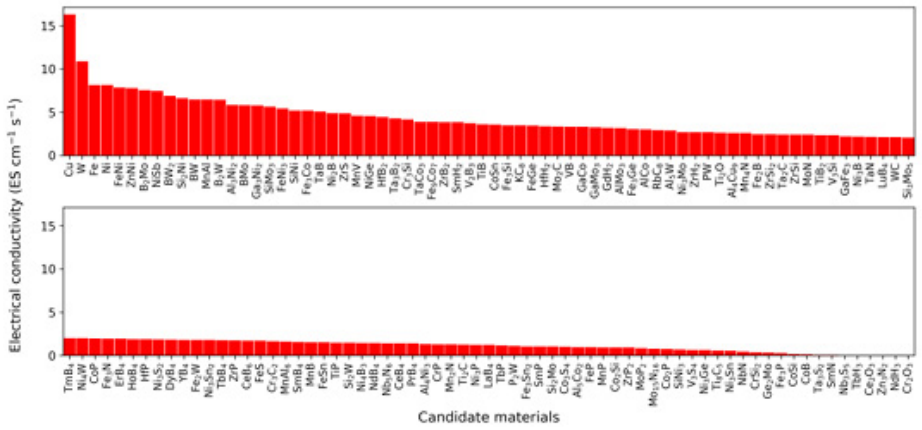

Figure 9. Electrical conductivity of the candidate materials for model (D). The electrical conductivity divided by the relaxation time is shown.